The cellular NMD pathway restricts Zika virus infection and is targeted by the viral capsid protein

Fontaine KA[1], Leon KE[1,2], Khalid MM[1], Jimenez-Morales D[1,3], Kaye J[1], Shah P[3,6], Finkbeiner S[1,4], Krogan N[1,3] and Ott M[1,5].

[1]Gladstone Institutes, San Francisco, CA, [2]Biomedical Sciences Graduate Program, University of California, San Francisco, CA, [3]Quantitative Biology Institute, Department of Cellular and Molecular Pharmacology, University of California, San Francisco, CA [4]Department of Neurology and Physiology, University of California, San Francisco, CA, [5]Department of Medicine, University of California, San Francisco, CA

[6]Present address: Departments of Chemical Engineering and Microbiology and Immunology, University of California, Davis, CA

Abstract

Zika virus (ZIKV) infection of neural progenitor cells (NPCs) *in utero* is associated with neurological disorders, such as microcephaly[1], but a detailed molecular understanding of ZIKV-induced pathogenesis is lacking. Here we show that *in vitro* ZIKV infection of human cells, including NPCs, causes disruption of the nonsense-mediated mRNA decay (NMD) pathway. NMD is a cellular mRNA surveillance mechanism that is required for normal brain size in mice[2-4]. Using affinity purification-mass spectrometry, we identified multiple cellular NMD factors that bind to the viral capsid protein, including the central NMD regulator up-frameshift protein 1 (UPF1)[5]. Endogenous UPF1 interacted with the viral capsid protein in co-immunoprecipitation experiments and capsid expression post-transcriptionally downregulated UPF1, a process that we confirmed occurs during *de*

novo* ZIKV infection. A further decrease in UPF1 levels by RNAi significantly enhanced ZIKV infection in NPC cultures. We therefore propose that ZIKV, via the capsid protein, has evolved a strategy to dampen antiviral activities of NMD[6,7], which subsequently contributes to neuropathology *in vivo.

Main

ZIKV is a mosquito-borne RNA virus that belongs to the *Flaviviridae* family. First isolated in Uganda in 1947, ZIKV remained relatively obscure for decades following its discovery because infection was associated with only mild disease. However, more severe clinical manifestations, including microcephaly, have been observed during the recent spread of ZIKV through the Americas[8]. While it is now established that ZIKV infection during pregnancy is a causative agent of microcephaly[9], the molecular mechanisms underlying ZIKV-induced neuropathogenesis remain largely unknown.

Microcephaly has been linked to genetic mutations that result in the impairment of the NMD pathway[2-4]. While NMD was initially found to serve as a quality control system that destroys transcripts containing premature termination codons, the pathway also targets a broader range of RNA substrates, including viral RNAs[5-7,10]. As ZIKV has an RNA genome, and we previously described perturbations of the NMD pathway in cells infected with hepatitis C virus[11], we hypothesized that ZIKV infection manipulates the cellular NMD pathway.

To determine if ZIKV infection affects NMD, we infected Huh7 human hepatic cells and human induced pluripotent stem cell (iPSC)-derived NPCs with ZIKV for 48 h. We isolated total RNA from infected cells and measured mRNA levels of three canonical NMD substrates: asparagine synthetase (ASNS), cysteinyl-tRNA synthetase (CARS), and SR protein SC35[11]. ASNS, CARS, and SC35 transcripts were significantly elevated in Huh7 cells and NPCs following infection with Asian lineage ZIKV strain P6-740 (Fig. 1a). Levels of NMD substrates were also elevated in Huh7 cells infected with the contemporary ZIKV clinical isolate

PRVABC59 (Puerto Rico, 2015)(Fig. 1a). We found that ZIKV-induced increase in NMD transcripts did not reflect a global increase in transcription, as mRNA levels of housekeeping genes, including glyceraldehyde 3-phosphate dehydrogenase (GAPDH), were not altered in infected cells (Fig. 1a). Together, these results indicate that ZIKV disrupts the NMD pathway during infection.

NMD substrates are regulated through the activity of UPF1, an evolutionarily conserved ATP-dependent RNA helicase. UPF1 plays a central role in the NMD pathway by linking the translation termination event to the assembly of a surveillance complex, resulting in NMD activation[12]. To determine if ZIKV infection more broadly affects NMD, we utilized two publicly available RNA-Seq datasets to compare genome-wide transcriptional alterations found during ZIKV infection[13] to those found following UPF1 knockdown[14]. As shown in Figure 1b, there is a significant overlap in upregulated genes between these two datasets. Interestingly, several of the overlapping genes are involved in cell cycle arrest and induction of apoptosis, two conditions linked to ZIKV-associated neuropathology[1]. These genes include DNA damage-inducible transcript 3 (DDIT3)[15] and growth arrest and DNA damage-inducible protein 45 alpha and beta (GADD45A and GADD45B, respectively)[16]. Via quantitative real-time RT-PCR, we confirmed that transcripts of each were upregulated following infection of Huh7 cells with ZIKV PRVABC59, while the mRNA levels of the housekeeping genes GAPDH, hypoxanthine phosphoribosyltransferase 1 (HPRT1), and lactate dehydrogenase A (LDHA) were not elevated (Fig. 1c). Combined, these data show that ZIKV infection is associated with dysregulated expression of NMD substrates relevant to ZIKV-mediated neuropathogenesis.

We previously showed that the core protein of HCV and capsid protein of the related flaviviruses dengue virus and West Nile virus interact with within bgcn homolog (WIBG/PYM1), a component of the exon junction complex (EJC) associated with NMD[11]. To examine potential interactions between ZIKV capsid and NMD-associated host factors, we used an affinity purification with mass spectrometry (AP-MS) approach to generate ZIKV capsid-host protein-

protein interaction (PPI) maps in HEK293T cells; ZIKV capsid from the Ugandan 1947 strain MR 766 or ZIKV capsid from the French Polynesian 2013 strain H/PF/2013 served as bait proteins (Shah et al., submitted). Three independent experiments were performed for each tagged ZIKV capsid bait protein, with tagged GFP and empty vector transfections used as negative controls. From these studies, we found that ZIKV capsid proteins interacted with several factors of the NMD pathway, including multiple members of the EJC complex, as well as UPF1 and UPF3B (UPF3B is an NMD effector that stimulates the helicase activity of UPF1) (Fig. 2a). Importantly, the NMD host factors that interact with each of the two different capsid proteins greatly overlapped, revealing that the interaction between capsid and the NMD pathway is conserved across the Asian and African lineages of ZIKV (Fig. 2a).

Next, we validated the binding of ZIKV capsid to UPF proteins by co-immunoprecipitating Flag-tagged capsid protein with endogenous UPF3B or UPF1 in HEK293T cells. Both UPF3B and UPF1 proteins co-immunoprecipitated with ZIKV capsid, confirming the AP-MS results (Fig. 2b,c, respectively). Surprisingly, we consistently observed a decrease in UPF1, but not UPF3B, protein levels in the input lysate of ZIKV capsid-transfected cells, pointing to a specific perturbation of UPF1 expression by ZIKV capsid (Fig. 2c). Because ZIKV capsid and UPF1 both localize to the nucleus and the cytoplasm[17,18], we also performed cellular fractionation studies in ZIKV capsid-transfected HEK293T cells. Capsid expression markedly decreased nuclear UPF1 levels, whereas cytoplasmic levels were unchanged (Fig. 2d). As UPF1 transcript levels are not altered in ZIKV-infected NPCs[13], and changes in UPF1 transcripts cannot explain the compartment–specific decrease in protein levels, we focused on mechanisms known to mediate nuclear degradation of proteins. Interestingly, nuclear UPF1 levels in capsid-transfected cells were not rescued by inhibition of either the ubiquitin-proteasome pathway via MG132 treatment or cellular autophagy via spautin-1 and bafilomycin A1 treatment, indicating that the mechanism of ZIKV capsid-mediated UPF1 protein downregulation is uncommon (Supplemental Fig. 1a,b, respectively). These data identified a

new interaction between ZIKV capsid and the NMD pathway that perturbs nuclear UPF1 levels through a yet-unknown mechanism. Notably, we detected no double-stranded viral RNA (dsRNA) in the nuclei of ZIKV-infected NPCs (Supplemental Fig. 2a,b and Supplemental Video 1), despite reports that flavivirus RNA or RNA replication is localized to the nucleus[19]. This suggested that UPF1 is not targeted by ZIKV capsid to protect nuclear viral RNA from degradation.

To confirm that UPF1 protein levels are dysregulated during *de novo* ZIKV infection, we performed western blot analysis of infected Huh7 cells and NPCs. Cellular UPF1 protein levels were consistently downregulated by ~50% in ZIKV-infected Huh7 cells, whereas a ~25% reduction was observed in ZIKV-infected NPCs (Fig. 3a,b, respectively). This difference in UPF1 downregulation mirrors the difference in infection efficiencies achieved in these two cell systems. As expected, UPF1 transcript levels were not lower in ZIKV-infected cells than in their mock-infected counterparts (Fig. 3c). In addition, no specific effect was observed on UPF1 phosphorylation, a mechanism known to activate UPF1[5], as the decrease detected in phosphorylated UPF1 levels corresponded with the reduction in total UPF1 levels in ZIKV-infected cells (Fig. 3d). These results confirm that UPF1 is post-transcriptionally downregulated during ZIKV infection.

We hypothesized that UPF1 serves as a restriction factor of ZIKV and is inactivated in infected cells to promote ZIKV propagation. To test this hypothesis, we decreased UPF1 expression prior to ZIKV infection by transfecting NPCs with either non-targeting siRNA or a pool of UPF1-specific siRNAs. We then infected the transfected cells with ZIKV and measured viral RNA levels, as well as infectious titers, 48 h post-infection (hpi). UPF1 knockdown was successful in siRNA-treated cells, as confirmed by western blot analysis (Fig. 4a). The depletion of UPF1 in NPCs prior to infection resulted in a significant increase in both ZIKV RNA replication and infectious virus production (Fig. 4b,c respectively), supporting the model that expression of UPF1 restricts ZIKV infection. Using confocal microscopy and 3D reconstruction analyses, we

observed no significant difference in the number and size of dsRNA foci when we compared ZIKV-infected, UPF1-depleted NPCs to ZIKV-infected cells expressing UPF1 (Fig. 4d). Instead, we found a consistent increase in the number of infected cells in NPC cultures when UPF1 was depleted (Fig. 4e), although this increase was not significant due to the variability in infection efficiencies across the two different NPC lines used. Combined, these data suggest that UPF1 expression renders NPCs more resistant to ZIKV infection, but does not target replicating viral RNA.

In summary, we identified the NMD pathway as a restriction mechanism for ZIKV infection in human NPCs. NMD was partially inactivated in ZIKV-infected NPCs through expression of the viral capsid protein and the resulting downregulation of host UPF1 protein levels. As weakening NMD by depleting UPF1 results in a marked increase in infection efficiency and favors successful ZIKV spread, we propose a model in which an “arms race” between cellular NMD and ZIKV determines whether a cell is successfully infected. The downregulation of UPF1 by capsid during ZIKV infection may be limited by potentially toxic effects of NMD impairment, as illustrated by the upregulation of genes regulating cell cycle growth arrest and apoptosis. Indeed, ZIKV-induced NMD impairment may contribute to severe neuropathology and microcephaly development, as documented in mice haploinsufficient for NMD factors[2-4]. Research is ongoing to determine the precise molecular mechanisms of ZIKV capsid-induced UPF1 downregulation and the specific role of nuclear UPF1 in ZIKV infection. This research may lead to new therapeutic approaches, as reinforcement of the antiviral properties of the cellular NMD pathway is expected to enhance resistance of NPCs to ZIKV infection and could promote normal neurodevelopment in infected fetuses.

Methods

Viruses and cells. Two Asian lineage strains of ZIKV, P6-740 (ATCC VR-1845) and PRVABC59 (ATCC VR-1843), were used for all experiments. ZIKV stocks were propagated in

Vero cells (ATCC) and titers were determined by plaque assays on Vero cells. Huh7 cells (ATCC) and Vero cells were maintained in Dulbecco's Modified Eagle's Medium (DMEM) with 10% fetal bovine serum (FBS), 2 mM L-glutamine, 100 U/mL penicillin, and 100 µg/mL streptomycin. HEK293T cells (ATCC) were maintained in DMEM/H21 medium supplemented with 10% FBS, 100 U/mL penicillin, 100 µg/mL streptomycin, and 1 mM sodium pyruvate or DMEM with 10% FBS, 2 mM L-glutamine, 100 U/mL penicillin, and 100 µg/mL streptomycin. Human iPSC-derived NPCs were generated and maintained as described previously[21]. All of the human fibroblast cell lines used to generate iPSCs came from the Coriell Institute for Medical Research. The iPSCs used in these studies were the CTRL2493nXX, CS2518nXX, and Cs71iCTR-20nXX lines. CTRL2493nXX was derived from the parental fibroblast line ND31845 that was biopsied from a healthy female at 71 years of age. The iPSC line was made by the Yale Stem Cell Center. CS2518nXX was derived from the parental fibroblast line ND30625 that was biopsied from a healthy male at 76 years of age. The iPSC line comes from the Coriell Institute for Medical Research. CS71iCTR-20nXX was derived from the parental fibroblast line ND29971 that was biopsied from a female at 61 years of age. This iPSC line comes from the Coriell Institute for Medical Research. For virus infections, NPCs plated on Matrigel-coated multi-well plates or Huh7 cells were infected with ZIKV at a multiplicity of infection of 0.1 or 1 for 2 h at 37°C. Infected cells were harvested at 48 hpi for all analyses.

Affinity purification, mass spectrometry, and AP-MS scoring. The ZIKV capsid open reading frames (ORFs) from the Ugandan 1947 strain MR 766 or the French Polynesian 2013 strain H/PF/2013 were cloned into pCDNA4_TO with a C-terminal 2xStrep II affinity tag for expression in human cells. The viral capsid proteins (three biological replicates), as well as GFP (two biological replicates) and empty vector (ten biological replicates) as negative controls, were expressed in HEK293T cells and affinity purifications were performed as previously described[21]. All lysates and affinity purified eluates were analyzed by western blot and silver stain PAGE to

confirm expression and purification. Purified protein eluates were digested with trypsin for LC-MS/MS analysis. Samples were denatured and reduced in 2M urea, 10 mM NH_4HCO_3, 2 mM DTT for 30 min at 60°C, then alkylated with 2 mM iodoacetamide for 45 min at room temperature. Trypsin (Promega) was added at a 1:100 enzyme:substrate ratio and digested overnight at 37°C. Following digestion, samples were concentrated using C18 ZipTips (Millipore) according to the manufacturer's specifications. Peptides were resuspended in 15 μL of 4% formic acid and 3% ACN, and 1-2 μL of sample was loaded onto a 75 μm ID column packed with 25 cm of Reprosil C18 1.9 μm, 120Å particles (Dr. Maisch). Peptides were eluted into a Q-Exactive Plus (Thermo Fisher) mass spectrometer by gradient elution delivered by an Easy1200 nLC system (Thermo Fisher). The gradient was from 4.5% to 32% acetonitrile over 53 minutes. All MS spectra were collected with oribitrap detection, while the 20 most abundant ions were fragmented by HCD and detected in the orbitrap. All data was searched against the SwissProt Human protein sequences, combined with ZIKV sequences and GFP. Peptide and protein identification searches, as well as label-free quantitation, were performed using the MaxQuant data analysis algorithm and all peptide and protein identifications were filtered to a 1% false-discovery rate[22,23]. SAINTq (PMID: 27119218) was used to calculate the probability of bait-prey interactions for both Ugandan ZIKV capsid and French Polynesian ZIKV capsid against the negative controls, including GFP and empty vector, with protein intensities as input values. We applied a combined threshold of probability of interaction (AvgP) greater than 0.90 and Bayesian False Discovery Rate of less than 0.05.

Quantitative real-time reverse transcription-PCR (qRT-PCR). Total cellular RNA was isolated from Huh7 cells and NPCs using the RNeasy Mini Kit (Qiagen). cDNA was synthesized with oligo$(dT)_{18}$ (ThermoFisher Scientific) primers, random hexamer (Life Technologies) primers, and AMV reverse transcriptase (Promega). The cDNA was then used in SYBR Green

PCR Master Mix (ThermoFisher Scientific) according to manufacturer's instructions and analyzed by qPCR (Bio-Rad ABI 7900). The primers used for ASNS, CARS, SC35 1.7, GAPDH, HPRT1, LDHA, and 18S rRNA have been described previously[11]. The additional primers used were ZIKV PRVABC59 forward primer 5'- GAG ACG AGA TGC GGT ACA GG -3', ZIKV PRVABC59 reverse primer 5'- CGA CCG TCA GTT GAA CTC CA -3', UPF1 forward primer 5'- CTG CAA CGG ACG TGG AAA TAC -3', UPF1 reverse primer 5'- ACA GCC GCA GTT GTA GCA C -3', DDIT3 forward primer 5'- CTG CTT CTC TGG CTT GGC TG -3', DDIT3 reverse primer 5'- GCT CTG GGA GGT GCT TGT GA -3', GADD45A forward primer 5'- GAG CTC CTG CTC TTG GAG AC -3', GADD45A reverse primer 5'- GCA GGA TCC TTC CAT TGA GA -3', GADD45B forward primer 5'- TGA CAA CGA CAT CAA CAT C -3', and GADD45B reverse primer 5'- GTG ACC AGA GAC AAT GCA G -3'. Relative levels of each transcript were normalized by the delta threshold cycle method to the abundance of 18S rRNA, with mock-infected cells set to 1.

Western blot analysis. Cells were lysed in RIPA lysis buffer (50mM Tris-HCl, pH 8, 150mM NaCl, 1% NP-40, 0.5% sodium deoxycholate, 0.1% SDS, supplemented with Halt™ protease inhibitor cocktail (ThermoFisher Scientific) to obtain whole cell lysates or lysed using the NE-PER nuclear and cytoplasmic extraction kit (ThermoFisher Scientific) to obtain cytoplasmic and nuclear fractions. Proteins were separated by SDS-PAGE and transferred to nitrocellulose membranes (Bio-Rad). Blots were incubated with the indicated primary antibody: anti-phospho-UPF1 (Ser1127) (07-1016, Millipore Sigma), anti-UPF1 (12040, Cell Signaling Technology, Inc.), anti-UPF3B (ab134566, Abcam), anti-ZIKV Envelope (E) (GTX133314, GeneTex), anti-ZIKV Capsid (C) (GTX133304, GeneTex), anti-Flag (F7425, Sigma-Aldrich), anti-SP1 (sc14027, Santa Cruz Biotechnology), anti-GAPDH (5174, Cell Signaling Technology, Inc.), anti-β-actin (A5316, Sigma-Aldrich). Proteins were visualized by chemiluminescent detection with ECL and

ECL Hyperfilm (Amersham). Differences in band intensity were quantified by densitometry using ImageJ.

Immunoprecipitations. Cells were lysed in either RIPA lysis buffer or IP lysis buffer (150mM NaCl, 50mM Tris pH 7.4, 1mM EDTA, 0.5% NP-40 substitute, supplemented with Halt™ protease inhibitor cocktail (ThermoFisher Scientific)) at 4°C and passed through a G23 needle. Clarified lysates were immunoprecipitated with Flag M2 agarose (Sigma) overnight, washed in lysis buffer, and resuspended in Laemmli buffer for SDS-PAGE. Western blot analysis of immunoprecipitated proteins was performed as described above.

Immunofluorescence. Transfected or infected NPCs were collected at 48 h and plated onto 22 × 22 mm #1.5 coverslips. Cells were fixed in 4% paraformaldehyde, permeabilized with 0.1% Triton X-100, and blocked in 3% bovine serum albumin. Cells were then immunostained with human anti-DENV mAb 1.6D (a generous gift from Sharon Isern and Scott Michael, Florida Gulf Coast University), which recognizes the ZIKV envelope protein or with the anti-dsRNA mAb J2 (SCICONS), and the appropriate secondary antibody. Coverslips were mounted onto glass slides using Vectashield® Mounting Medium with DAPI (Vector Laboratories) and analyzed by fluorescence microscopy (Zeiss Axio Observer ZI) or confocal microscopy (Zeiss LSM 880). For acquiring high-resolution images, cells were imaged on the Zeiss LSM 880 with Airyscan using a 20x/0.8 or 63x/1.4 M27 oil immersion objective. A total of 15-20 (20x objective) or 60-80 (63x objective) Z-slices were acquired every 0.88 µm or 0.3 µm, respectively. The resulting Z-stack was reconstructed and rendered in three dimensions using Imaris software (Bitplane). The Imaris co-localization function was used to determine overlap of DAPI and dsRNA fluorescence. dsRNA foci were reconstructed via the Imaris spot detection function, which provided an analysis of total number and mean volume of foci within a cell.

Statistical analysis. Statistical differences between groups were analyzed using either a two-tailed unpaired Student's *t*-test or a two-tailed ratio paired Student's *t*-test, as stated in the figure legends. Hypergeometrical tests were used to calculate the probability of an overlap in gene dysregulation between ZIKV-infected NPCs and UPF1-depleted cells and to calculate the probability of ZIKV capsid bait-prey interactions. Data are represented as mean ± s.e.m. Statistical significance was defined as $*P \leq 0.05$, $**P \leq 0.01$, $***P \leq 0.001$, and $****P \leq 0.0001$.

Acknowledgements. The authors would like to thank all members of the Ott laboratory, as well as Roman Camarda and Marius Walter, for helpful discussions and advice throughout the preparation of this manuscript. We thank the Gladstone Stem Cell Core, the Gladstone Microscopy Core, and Mariah Dunlap for technical assistance and Drs. Sharon Isern and Scott Michael (Florida Gulf Coast University) for reagents. We are grateful to Veronica Fonseca and John Carroll for administrative and graphical support, respectively, and to Eric Martens and Gary Howard for editorial assistance. This work was supported by NIH/NIAID F32AI112262 to P.S.S., NIH/NINDS R01 NS101996-01 to S.F., NIH/NIAID U19AI1186101 to N.J.K., DOD/DARPA HR0011-11-C-0094 (PROPHECY) to N.J.K., NIH/NIAI R01 AI097552 to M.O., and the James B. Pendleton Charitable Trust.

Competing interests. The authors declare no competing financial interests.

Author contributions. K.A.F., K.E.L., M.K., and P.S. designed, conducted, and analyzed the experiments. D.J. performed the bioinformatics analyses and provided graphical support. M.O. supervised, guided, and funded the project. J.K., S.F., and N.J.K. provided critical reagents and technical guidance. The manuscript was written by K.A.F., K.E.L., and M.O. with input from N.J.K.

Figure Legends

Figure 1. The NMD pathway is disrupted during ZIKV infection.

(a) Transcript levels of NMD substrates and housekeeping genes from Huh7 cells or NPCs mock-infected or infected with ZIKV strain P6-740 or the contemporary clinical isolate PRVABC59. Cells were infected at a multiplicity of infection (MOI) of 0.1 or 1 and harvested at 48 hours post-infection (hpi). Data are represented as mean ± s.e.m. *P* values were calculated by unpaired Student's *t*-test. **P* ≤ 0.05; ***P* ≤ 0.01; ns, not significant. n= 3 independent experiments.

(b) Venn diagram showing overlap of significantly upregulated genes associated with ZIKV infection of NPCs and UPF1 knockdown in HeLa cells. RNA-Seq analyses of mock-infected or ZIKV-infected NPCs harvested at 56 hpi and control siRNA-treated or UPF1 siRNA-treated HeLa TO cells harvested at 72 hours post-transfection (hpt). The GeneProf hypergeometric probability calculator (http://www.geneprof.org/GeneProf/tools/hypergeometric.jsp) was then used to generate a hypergeometric *P* value. *****P* ≤ 0.0001.

(c) Transcript levels of housekeeping genes and select genes involved in cell cycle growth arrest and apoptosis that were identified in (b). Huh7 cells were mock-infected or infected with ZIKV PRVABC59 at an MOI of 0.1 or 1 and harvested at 48 hpi. Data are represented as mean ± s.e.m. *P* values were calculated by unpaired Student's *t*-test. **P* ≤ 0.05; ***P* ≤ 0.01; ****P* ≤ 0.001; ns, not significant. n= 3 independent experiments.

Figure 2. The capsid protein of ZIKV interacts with the NMD pathway and downregulates UPF1.

(a) PPI maps of ZIKV capsid (Ugandan (Ug Cap), MR 677; French Polynesian (Fp Cap), H/PF/2013) and identified NMD factors. Aquamarine or turquoise lines indicate interactions between the ZIKV capsid proteins and host NMD factors. Curated host-host protein interactions

from the CORUM database are indicated by the grey lines. *P* values were calculated using hypergeometrical tests (Ug Cap, $P = 3.45 \times 10^{-7}$; Fp Cap, $P = 7.16 \times 10^{-10}$).

(b) Flag-tag co-immunoprecipitation (co-IP) and western blot analysis of HEK293T cells transfected with vector or Flag-tagged ZIKV capsid (H/PF/2013, Asian lineage) and harvested at 48 hpt to immunoprecipitate endogenous UPF3B. The upper band detected in the IP Capsid blot represents a non-specific artifact.

(c) Co-IP and western blot analysis of HEK293T cells transfected with vector or Flag-tagged ZIKV capsid (H/PF/2013, Asian lineage) and harvested at 48 hpt to immunoprecipitate endogenous UPF1.

(d) Western blot analysis of UPF1 levels in subcellular fractionated HEK293T cells transfected with vector or Flag-tagged ZIKV capsid (H/PF/2013, Asian lineage) for 48 h. GAPDH was used as a cytoplasmic marker and SP1 as a nuclear marker to ensure optimal fractionation. Densitometric analyses were performed using ImageJ to quantify relative band intensities. Data are represented as mean ± s.e.m. *P* values were calculated by unpaired Student's *t*-test. $^{**}P \leq 0.01$; ns, not significant. n= 3 independent experiments.

Figure 3. UPF1 is post-transcriptionally downregulated during ZIKV infection.

(a) Western blot analysis of UPF1 levels in mock-infected and ZIKV-infected (PRVABC59, MOI of 1) Huh7 cells harvested at 48 hpi, with β-actin and ZIKV envelope protein (ZIKV E) serving as loading and infection controls, respectively. Densitometric analyses were performed using ImageJ to quantify relative band intensities. Data are represented as mean ± s.e.m. *P* values were calculated by unpaired Student's *t*-test. $^{**}P \leq 0.01$. n= 3 independent experiments.

(b) Western blot analysis of UPF1 levels in mock-infected and ZIKV-infected (P6-740, MOI of 1) NPCs harvested at 48 hpi, with β-actin and ZIKV capsid protein (ZIKV C) serving as loading and infection controls, respectively. Densitometric analyses were performed using ImageJ to quantify relative band intensities. Data are represented as mean ± s.e.m. *P* values were

calculated by unpaired Student's *t*-test. ***$P \leq 0.001$. n= 3 independent experiments using one NPC line.

(c) UPF1 transcript levels from Huh7 cells mock-infected or infected with ZIKV strain PRVABC59 at an MOI of 0.1 or 1 and harvested at 48 hpi. Data are represented as mean ± s.e.m. *P* values were calculated by unpaired Student's *t*-test. ns, not significant. n= 3 independent experiments.

(d) Western blot analysis of phosphorylated (p-UPF1) and total levels of UPF1 in mock-infected and ZIKV-infected (PRVABC59, MOI of 1) Huh7 cells harvested at 48 hpi, with β-actin and ZIKV E serving as loading and infection controls, respectively.

Figure 4. UPF1 is a restriction factor of ZIKV.

(a) Western blot analysis of UPF1 levels in NPCs transfected with non-targeting siRNA (siNT) or a pool of UPF1-specific siRNAs (siUPF1) at 96 hpt. Densitometric analyses were performed using ImageJ to quantify relative band intensities. Data are represented as mean ± s.e.m. *P* value was calculated by unpaired Student's *t*-test. **$P \leq 0.01$. n= 3 independent experiments using one NPC line.

(b) ZIKV RNA levels in siNT-treated or siUPF1-treated NPCs infected with ZIKV strain PRVABC59 at an MOI of 0.1 or 1 and harvested at 48 hpi. Data are represented as mean ± s.e.m. *P* value was calculated by two-tailed ratio paired Student's *t*-test. ***$P \leq 0.001$.

(c) Released infectious virus from siNT-treated or siUPF1-treated, ZIKV-infected (PRVABC59, MOI of 1) NPCs harvested at 48 hpi. Data are represented as mean ± s.e.m. *P* value was calculated by unpaired Student's *t*-test. **$P \leq 0.01$. n= 3 independent experiments using one NPC line.

(d) Representative confocal microscopy images of a ZIKV-infected, siNT-treated NPC or a ZIKV-infected, siUPF1-treated NPC with the nuclei stained with DAPI and ZIKV dsRNA foci stained with the anti-dsRNA mAb J2. Three-dimensional image rendering and reconstructed

dsRNA foci were produced using the Imaris spot detection function. Measurements of dsRNA foci count and volume were averaged for each cell. Data are represented as mean ± s.e.m. n = 3 independent experiments using two NPC lines. Scale bar represents 2 μm.

(e) Infection rates of siNT-treated or siUPF1-treated, ZIKV-infected (PRVABC59, MOI of 1) NPCs measured at 48 hpi. Fixed cells were subjected to the anti-DENV mAb 1.6D, which also recognizes the ZIKV envelope protein. Data are represented as mean ± s.e.m. n = 3 independent experiments using two NPC lines.

Supplemental Figure 1. ZIKV capsid-induced nuclear UPF1 downregulation occurs via a proteasome- and autophagy-independent mechanism.

(a) Western blot analysis of nuclear UPF1 levels in fractionated HEK293T cells transfected with vector or Flag-tagged ZIKV capsid for 48 h. Cells were treated with DMSO or the proteasome inhibitor MG132 (20 μM) for 4 h before harvest.

(b) Western blot analysis of nuclear UPF1 levels in fractionated HEK293T cells transfected with vector or Flag-tagged ZIKV capsid for 48 h. Cells were treated with DMSO or the autophagy inhibitors spautin-1 (SP-1) (10 μM) or bafilomycin A1 (BAF) (10 nM) for 24 h before harvest.

Supplemental Figure 2. ZIKV RNA is not localized to the nucleus during infection.

(a) Representative confocal microscopy images of a ZIKV-infected NPC (PRVABC59, MOI of 1) showing antibody-stained dsRNA fluorescence and dsRNA foci as reconstructed by the Imaris spot detection function. The overlay of the two images shows concordance of the dsRNA signal. Scale bar represents 2 μm.

(b) Representative confocal microscopy images of a mock-infected NPC and ZIKV-infected (PRVABC59, MOI of 1) NPC. The pink dsRNA foci denote overlap of dsRNA fluorescence and DAPI fluorescence. Scale bar represents 3 μm.

Supplemental Video 1. ZIKV RNA is not localized to the nucleus during infection. Representative three-dimensional video of rendered confocal Z-stacks of a ZIKV-infected NPC (PRVABC59, MOI of 1), with dsRNA fluorescence reconstructed as foci by the Imaris spot detection function. Scale bar represents 2 μm.

References

1. Li, C. *et al*. Zika Virus Disrupts Neural Progenitor Development and Leads to Microcephaly in Mice. *Cell Stem Cell* **19**, 120-126 (2016).

2. Silver, D. L. *et al*. The exon junction complex component Magoh controls brain size by regulating neural stem cell division. *Nat. Neurosci.* **13**, 551-558 (2010).

3. Mao, H., McMahon, J. J., Tsai, Y., Wang, Z. & Silver, D. L. Haploinsufficiency for Core Exon Junction Complex Components Disrupts Embryonic Neurogenesis and Causes p53-Mediated Microcephaly. *PLoS Genetics* **12**, e1006282 (2016).

4. Mao, H. *et al*. Rbm8a haploinsufficiency disrupts embryonic cortical development resulting in microcephaly. *J. Neurosci.* **35**, 7003-7018 (2015).

5. Brogna, S. & Wen, J. Nonsense-mediated mRNA decay (NMD) mechanisms. *Nature Structural & Molecular Biology* **16**, 107-113 (2009).

6. Jerome M Molleston & Sara Cherry. Attacked from All Sides: RNA Decay in Antiviral Defense. *Viruses* **9**, 2 (2017).

7. Rigby, R. E. & Rehwinkel, J. RNA degradation in antiviral immunity and autoimmunity. *Trends in Immunology* **36**, 179-188 (2015).

8. Fauci, A. S. & Morens, D. M. Zika Virus in the Americas--Yet Another Arbovirus Threat. *N. Engl. J. Med.* **374**, 601-604 (2016).

9. Rasmussen, S. A., Jamieson, D. J., Honein, M. A. & Petersen, L. R. Zika Virus and Birth Defects — Reviewing the Evidence for Causality. *N. Engl. J. Med.* **374**, 1981-1987 (2016).

10. Balistreri, G., Bognanni, C. & Mühlemann, O. Virus Escape and Manipulation of Cellular Nonsense-Mediated mRNA Decay. *Viruses* **9** (2017).

11. Ramage, H. R. *et al*. A combined proteomics/genomics approach links hepatitis C virus infection with nonsense-mediated mRNA decay. *Mol. Cell* **57**, 329-340 (2015).

12. Hug, N., Longman, D. & Cáceres, J. F. Mechanism and regulation of the nonsense-mediated decay pathway. *Nucleic Acids Res.* **44**, 1483-1495 (2016).

13. Tang, H. *et al*. Zika Virus Infects Human Cortical Neural Progenitors and Attenuates Their Growth. *Cell Stem Cell* **18**, 587-590 (2016).

14. Tani, H. *et al*. Identification of hundreds of novel UPF1 target transcripts by direct determination of whole transcriptome stability. *RNA Biology* **9**, 1370-1379 (2012).

15. Jauhiainen, A. *et al*. Distinct cytoplasmic and nuclear functions of the stress induced protein DDIT3/CHOP/GADD153. *PLoS ONE* **7**, e33208 (2012).

16. Salvador, J. M., Brown-Clay, J. D. & Fornace, A. J. Gadd45 in stress signaling, cell cycle control, and apoptosis. *Adv. Exp. Med. Biol.* **793**, 1-19 (2013).

17. Varsally, W. & Brogna, S. UPF1 involvement in nuclear functions. *Biochem. Soc. Trans.* **40**, 778-783 (2012).

18. Lukasz P Slomnicki *et al*. Ribosomal stress and Tp53-mediated neuronal apoptosis in response to capsid protein of the Zika virus. *Scientific Reports (Nature Publisher Group)* **7**, 1-15 (2017).

19. Adam J Lopez-Denman & Jason M Mackenzie. The IMPORTance of the Nucleus during Flavivirus Replication. *Viruses* **9**, 14 (2017).

20. Developmental alterations in Huntington's disease neural cells and pharmacological rescue in cells and mice. *Nat. Neurosci.* **20**, 648-660 (2017).

21. Jäger, S. *et al*. Purification and characterization of HIV-human protein complexes. *Methods* **53**, 13-19 (2011).

22. Cox, J. *et al*. Accurate proteome-wide label-free quantification by delayed normalization and maximal peptide ratio extraction, termed MaxLFQ. *Mol. Cell Proteomics* **13**, 2513-2526 (2014).

23. Cox, J. & Mann, M. MaxQuant enables high peptide identification rates, individualized p.p.b.-range mass accuracies and proteome-wide protein quantification. *Nat. Biotechnol.* **26**, 1367-1372 (2008).

Figure 1

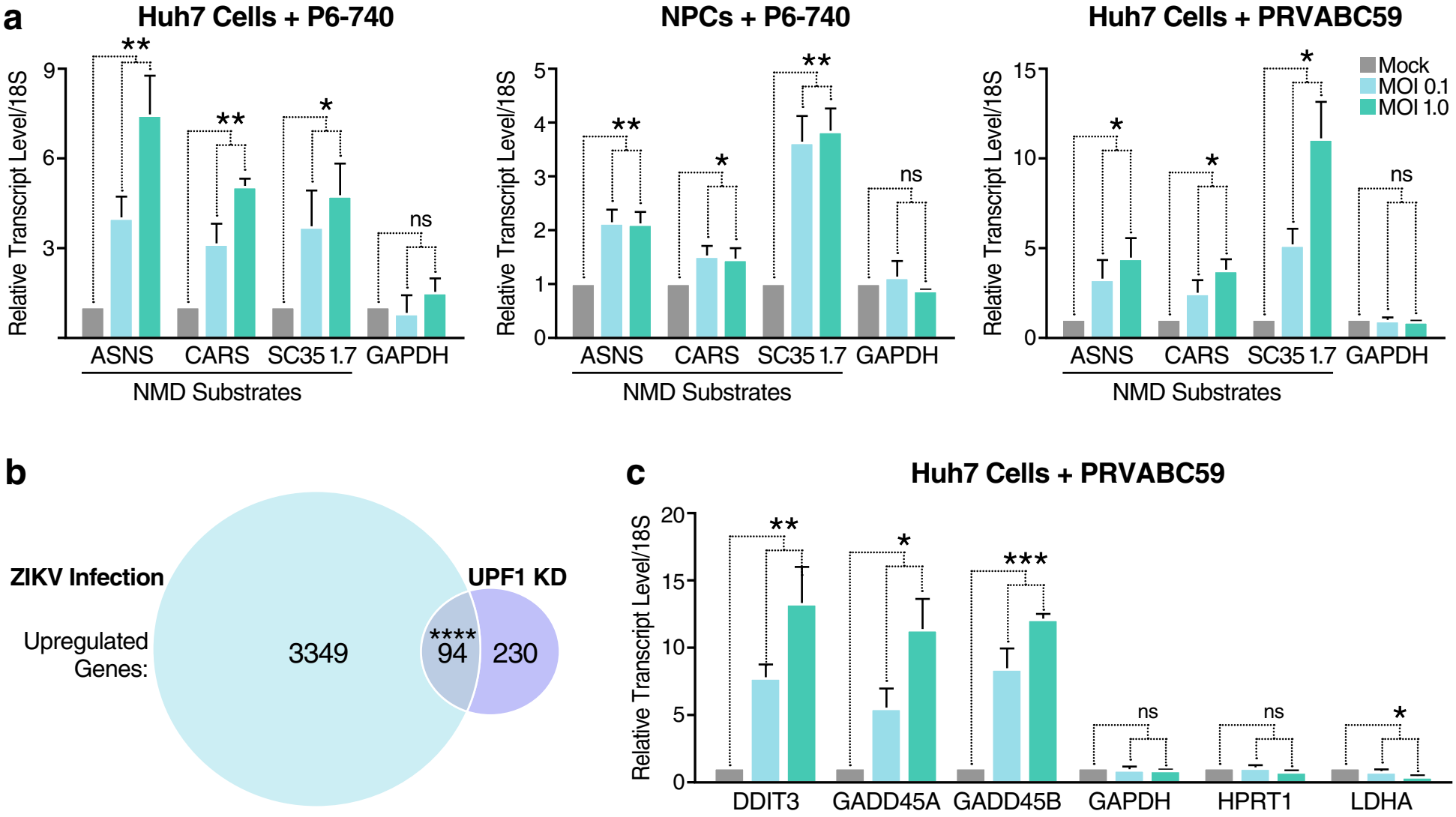
a
Huh7 Cells + P6-740
NPCs + P6-740
Huh7 Cells + PRVABC59
Relative Transcript Level/18S
Mock
MOI 0.1
MOI 1.0
ASNS
CARS
SC35 1.7
GAPDH
NMD Substrates
ns
b
ZIKV Infection
UPF1 KD
Upregulated Genes:
3349
****
94
230
c
Huh7 Cells + PRVABC59
Relative Transcript Level/18S
DDIT3
GADD45A
GADD45B
GAPDH
HPRT1
LDHA

Figure 2

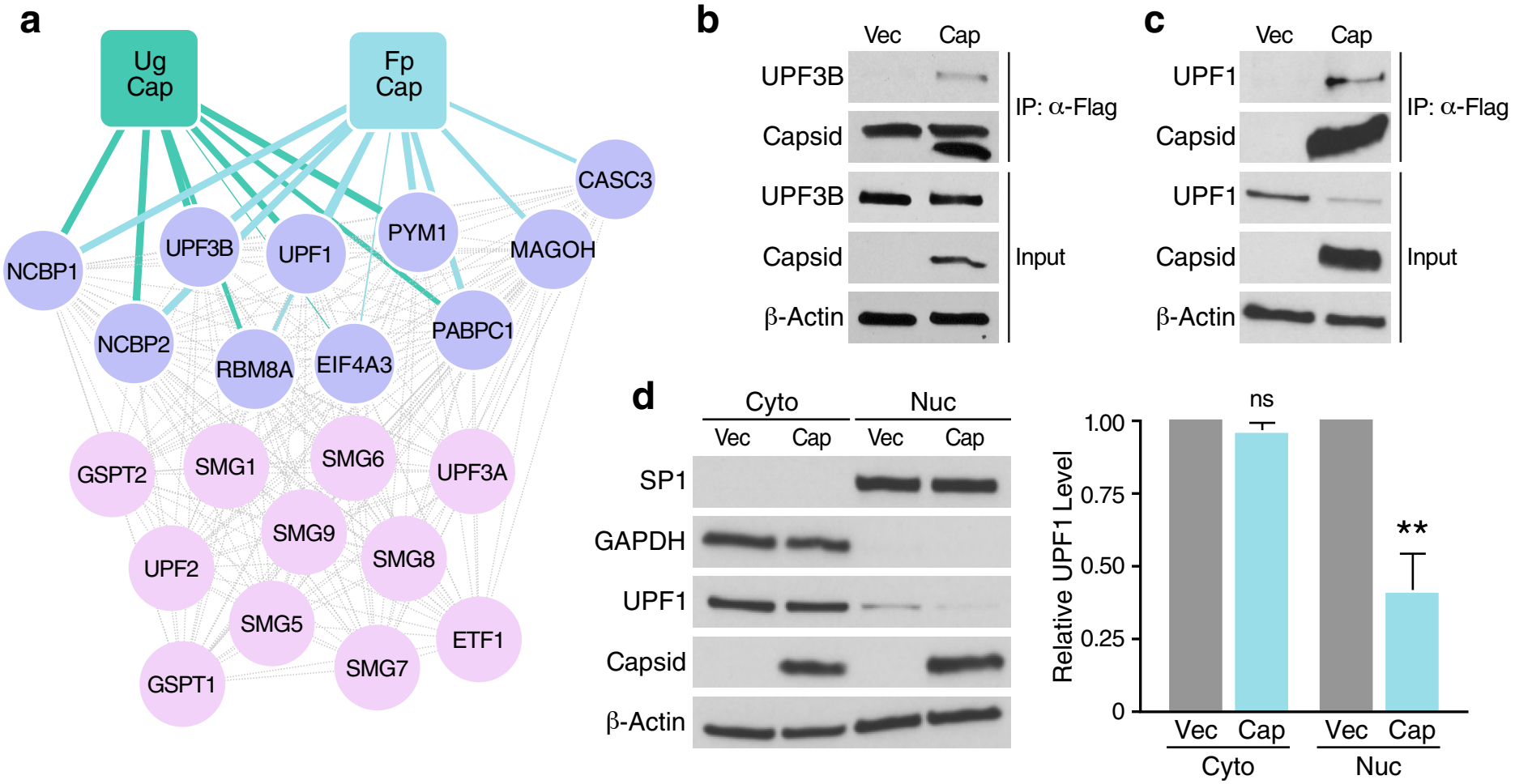
a
Ug Cap
Fp Cap
CASC3
NCBP1
UPF3B
UPF1
PYM1
MAGOH
NCBP2
RBM8A
EIF4A3
PABPC1
GSPT2
SMG1
SMG6
UPF3A
SMG9
UPF2
SMG8
SMG5
ETF1
GSPT1
SMG7
b
Vec
Cap
UPF3B
Capsid
IP: α-Flag
UPF3B
Capsid
Input
β-Actin
c
Vec
Cap
UPF1
Capsid
IP: α-Flag
UPF1
Capsid
Input
β-Actin
d
Cyto
Nuc
Vec
Cap
Vec
Cap
SP1
GAPDH
UPF1
Capsid
β-Actin
ns
**
Relative UPF1 Level
1.00
0.75
0.50
0.25
0
Vec
Cap
Vec
Cap
Cyto
Nuc

Figure 3

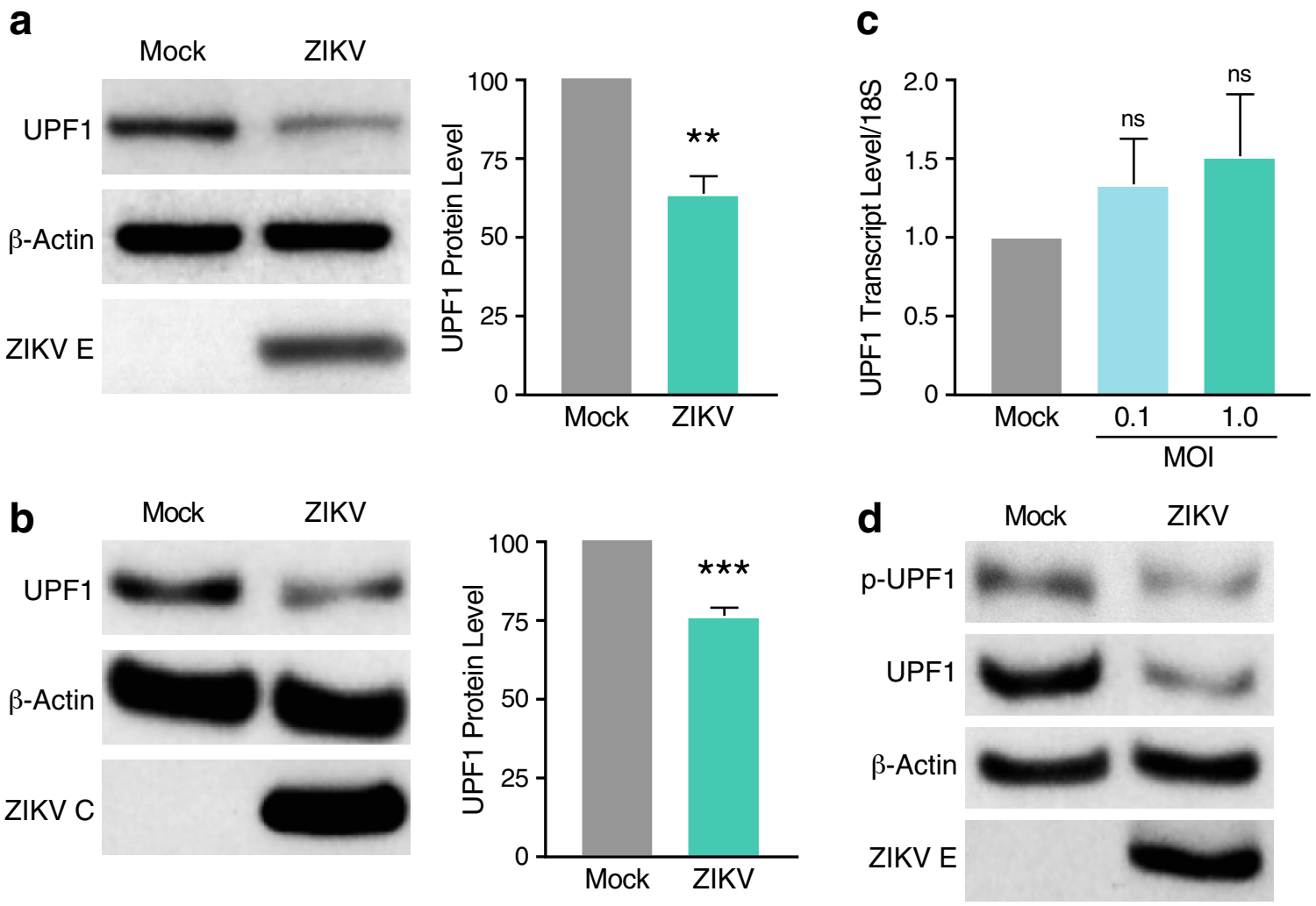
a
Mock
ZIKV
UPF1
β-Actin
ZIKV E
UPF1 Protein Level
100
75
50
25
0
**
Mock
ZIKV
b
Mock
ZIKV
UPF1
β-Actin
ZIKV C
UPF1 Protein Level
100
75
50
25
0
***
Mock
ZIKV
c
UPF1 Transcript Level/18S
2.0
1.5
1.0
0.5
0
ns
ns
Mock
0.1
1.0
MOI
d
Mock
ZIKV
p-UPF1
UPF1
β-Actin
ZIKV E

Figure 4

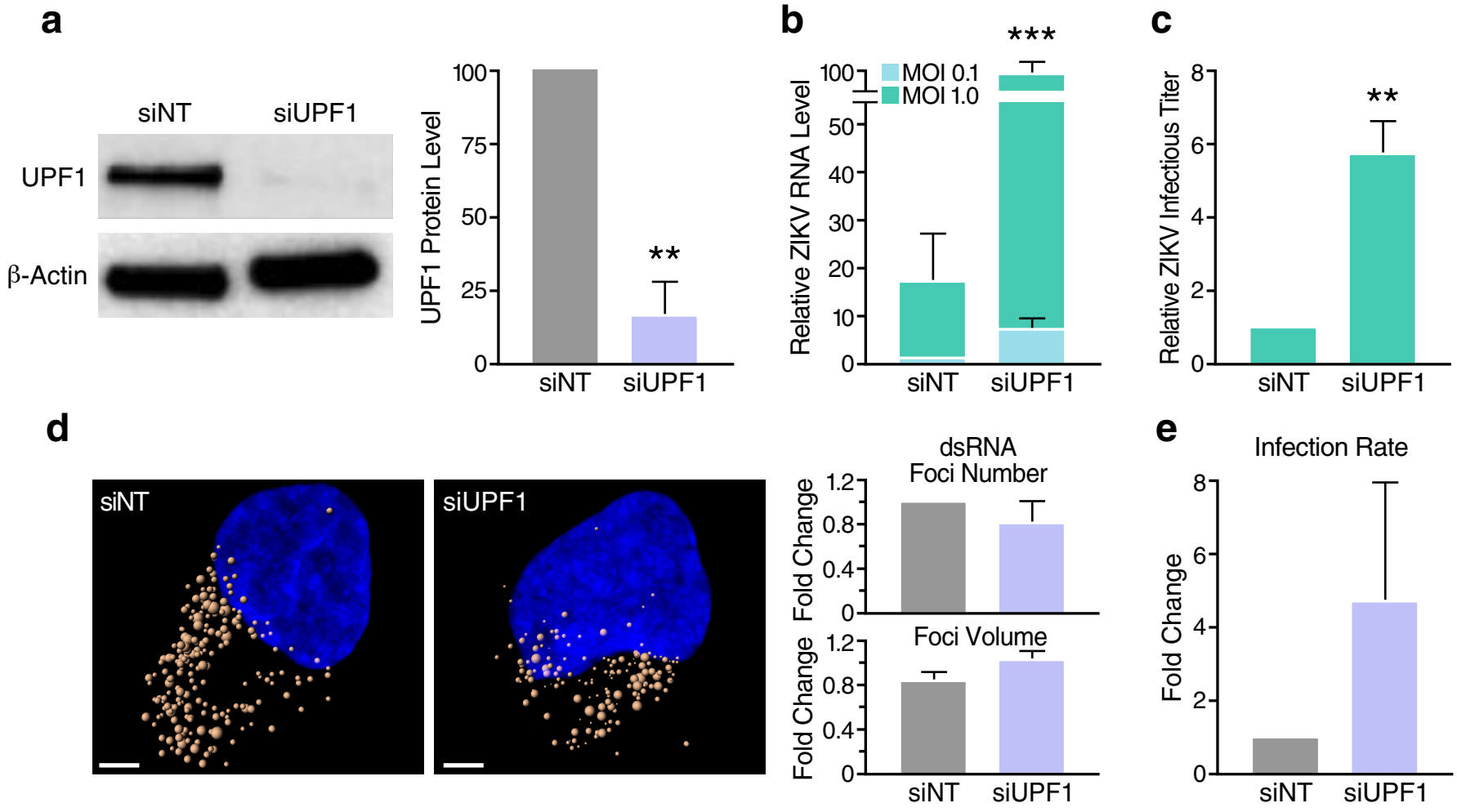
a
siNT
siUPF1
UPF1
β-Actin
UPF1 Protein Level
100
75
50
25
0
**
siNT
siUPF1
b
***
MOI 0.1
MOI 1.0
Relative ZIKV RNA Level
100
50
40
30
20
10
0
siNT
siUPF1
c
Relative ZIKV Infectious Titer
8
6
4
2
0
**
siNT
siUPF1
d
siNT
siUPF1
dsRNA
Foci Number
Fold Change
1.2
0.8
0.4
0
Foci Volume
Fold Change
1.2
0.8
0.4
0
siNT
siUPF1
e
Infection Rate
Fold Change
8
6
4
2
0
siNT
siUPF1